Atomistic modeling of the electrostatic and transport properties of a simplified nanoscale field effect transistor

Li-Na Zhao, Xue-Feng Wang,* Zhen-Hua Yao, Zhu-Feng Hou, and Marcus Yee

Atomistix Asia Pacific Pte Ltd, Unit 106, 16 Nanyang Drive, NTU Singapore 637722

Xing Zhou, Shi-Huan Lin, and Teck-Seng Lee

School of Electrical and Electronic Engineering, Nanyang Technological University, Nanyang Avenue, Singapore 639798

(Dated: November 29, 2008)

A first-principle model is proposed to study the electrostatic properties of a double-gated silicon slab of nano scale in the framework of density functional theory. The applied gate voltage is approximated as a variation of the electrostatic potential on the boundary of the supercell enclosing the system. With the electron density estimated by the real space Green's functions, efficient multigrid and fast Fourier Poisson solvers are employed to calculate the electrostatic potential from the charge density. In the representation of localized SIESTA linear combination of atomic orbitals, the Kohn-Sham equation is established and solved self-consistently for the wavefunction of the system in the local density approximation. The transmission for ballistic transport across the atomic silicon slab at small bias is calculated. The charge distribution and electrostatic potential profile in the silicon slab versus the gate voltage are then analyzed with the help of the equivalent capacitive model. Quantum confinement and short gate effects are observed and discussed.

PACS numbers:

I. INTRODUCTION

The size of Si based metal-insulator-semiconductor (MIS) devices has been shrunk aggressively to nanoscale nowadays [1] in design of very large scale integrated circuits. The quantum-mechanical nature of transport becomes inevitably prominent and there are extensive efforts devoted to modeling quantum behaviors in nano-MIS devices based on the effective mass approximation or the empirical tight-binding models. [2, 3, 4, 5, 6, 7, 8, 9, 10] Besides the traditional top-down technologies, bottom-up techniques has also been developed to fabricate Si nanostructures such as nanowires for future nanodevices. [11] As a result, the first-principle study on electronic and transport properties of atomic Si systems becomes attractive. [12, 13]

Due to the extensive application of Si based field effect transistors, some efforts have been carried out to the first-principle understanding of their behaviors in the past years. Evans et al. [14] have studied the effect of Si-SiO$_2$ interface roughness on the electron mobility in a Si based MIS structure by describing the roughness by first principles. Based on the above method, Hadjisavvas et al. [15] have proposed an explanation for electron mobility enhancement in strained MIS field effect transistors (FETs). Fonseca et al. [16] and Liu et al. [17] have established a two-terminal system of Si-HfO$_2$-Si and Al-SiO$_2$-nSi respectively described by a self-consistent density functional theory (DFT) and studied the transport properties through the HfO$_2$ and SiO$_2$ slab in the framework of the nonequilibrium Green's function (NEGF). In

this way, they have estimated the leakage current through the ultra-thin oxide barriers of MISFETs as a function of the voltage drop. Landman et al. [18] have studied the quantum transport through short Si nanowires passivated by hydrogen atoms and attached between Al electrodes by solving the eigenchannels of the scattering states in the framework of the density functional method with plan wave basis. Similarly, Ng et al. [19] studied the quantum transport through hydrogenated Si nanowires with Li electrodes employing the NEGF-DFT approach integrated in the Atomistix ToolKit (ATK) package. Fernández-Serra et al. [20] have investigated the effect of doping on electronic quantum transport in Si nanowires by assuming the same material (Si) for electrodes and the device regions. Later on, Markussen et al. [21] have continued the work for longer wires and studied the crossover from ballistic to diffusive transport based on the DFT and a recursive Green's function approach. Besides the above two-terminal models, three terminal models have also been used for Si systems to take into account the gate effect. Using the NEGF-DFT approach with the help of ATK package, Dai et al. [22] have investigated the transport properties of a Si$_4$ cluster sandwiched between two Al electrodes. By assuming a constant potential shift in the molecular region [23, 24] when a gate voltage is applied to the third terminal, they have observed charge transfer from the molecular and transconductance oscillation.

The aim of this work is to go further from small three-terminal molecular systems to more realistic multiterminal MIS devices of nanoscale using the NEGF-DFT approach. However, a rigorous treatment [25] of realistic multiterminal systems is computationally too expensive. Fortunately, particle exchange between the gate and the channel is usually very limited as they are separated by

---

*corresponding author: xw@atomistix.com

the insulator slab and the gate terminal works as a controller of electrostatic potential in the device region. To assure the simulation feasible with the present computation capability while catching the most important characteristics of nano MISFETs, we use a simplified model and focus ourselves on the gate effects on the electrostatic and transport properties under a small source-drain bias (in the linear region). As we know, in a real MIS device, how the gate voltage is distributed into the channel of the device or the electrostatic property of the device as a MIS capacitor is critical in determining the characteristics of the whole device. [26] For example, double-gate (DG) structure has been considered as the most promising device geometrical structure for nano MIS devices due to its good electrostatic integrity [27, 28]. In our model, we will take the effect of gate voltage distribution into account instead of simply adding a constant shift to the electrostatic potential. The gate voltage that controls the boundary condition and the corresponding variation of potential inside the device is self-consistently determined by Poisson equation.

The rest of the paper is organized as follows. In Sec. II, we define the device model and briefly describe the NEGF-DFT formalism and the computation method. In Sec. III, the result for electrostatic properties, charge and potential, are reported and analyzed with the help of density of states (DOS) and transmission spectra. Finally, a brief summary is given in Sec. IV.

II. MODEL AND METHOD

A. Device Model

We consider a prototype DG MISFET as schematically shown in Fig. 1(a). The device is made from a Si slab with thickness of nm order in the x direction. The channel (z) direction is chosen along Si crystal [001] orientation and the interfaces along (100) which is the preferred direction due to lower interface defect density and higher mobility. H atoms are used to passivate the dangling Si bonds on the surfaces. The H-Si bond length is relaxed and has a value of 1.49 Å while the Si-Si bond length is 2.35 Å. Further on either side of the Si slab a metal gate of variable length along z direction is located a few angstroms away from the H atom sheet, as indicated by the thick solid bars in Fig. 1(a). Note that here we insert the vacuum slabs, instead of oxide slabs, between the gates and the Si slab as the insulator. This is one of the simplifications introduced in this model in order to reduce the computation load. Since the dielectric constant of vacuum ($\kappa_v = 1$) is much lower than that of oxide (e.g. $\kappa_{ox} = 3.9$ for SiO$_2$), we expect a lower insulator capacitance (between the gate and the channel) in our model and, hence, a larger gate threshold than that for devices with oxide insulator slabs.

Four different model structures of total length 21.72 Å are studied in this paper and they are denoted as S_{mn} for models with short gate (length 5.43 Å) and L_{mn} for the model with long gate (in the full central region of length 10.86 Å). The index m (n) is used to distinguish models with different thickness of the Si slab (vacuum slab). The Si slab in the models is m unit-cells thick (5.43 and 10.86 Å for $m = 1$ and 2 respectively). The corresponding vacuum slab thickness is 1.9 and 2.9 Å for $n = 1$ and 2 respectively.

Another simplification is to approximate the gate effect with a boundary condition based on the following physical consideration. When we apply a small voltage drop between the Si slab and the metal gates we shift the Fermi energy in the latter by letting the former grounded. Due to the high electron density in metal, the electrostatic potential in the gates will shift in parallel with the gate Fermi energy or the voltage drop. As a result, the role of the metal gates on the channel is to control the electrostatic boundary of the supercell as enclosed by the solid lines in Fig. 1(a). Understanding this gating mechanism, we can exclude the gate materials from our model system (inside the supercell) while taking its most important effect into account by shifting the boundary condition as further explained in next section.

A third simplification is to use the same material for the source/drain electrodes and the channel. In real MISFET devices, the drain and source electrodes are doped and the contact between the electrodes and the channel adds to the complexity of the system and makes the result difficult to analyze. In this work, we focus on the gating effect in the channel region and it would be more practical to handle a simplified system. This simplification is expected not to affect the conclusion when the bias is low and has been used by other authors. [20]

After the above simplifications, in our model, the double-gated MISFET is a Si slab with known electrostatic boundary and can be studied by the NEGF-DFT method. The system is composed of a hydrogen passivated Si slab and two vacuum slabs. Along z axis, as separated by the vertical dash lines in Fig. 1(a), the system is divided into three regions: the left electrode (L) the central region, or the channel region (C), and the right electrode (R). In z direction, the electrostatic potential of a Si slab without gate is used as the boundary condition of the electrostatic potential on the left and right boundaries of the supercell. This implies that the left and right electrodes are assumed semi-infinite. In y direction, the periodic boundary condition is applied to assume an extending system in this direction. In x direction, the boundary is variable depending on the system size and the gate voltage and will be specified in the corresponding context. Furthermore, we assume a uniform Fermi level inside the supercell. This approximation is justified in case of small bias between the source and drain electrodes because the gate voltage induced variation of Fermi energy happens mainly in the vacuum slab and the density of states there is negligible.
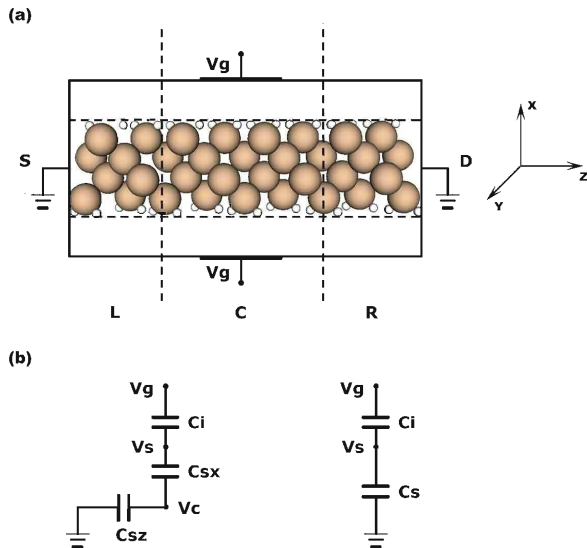
FIG. 1: (a) Atomistic scheme of a model double-gate MIS-FET enclosed in one supercell of length 21.72 Å (four Si unit cells). The system has the left electrode (L), the central region (C), and the right electrode (R) separated by the vertical dashed lines at $z = 5.43$ and 16.29 Å. The atomic positions projected to the x-z plane are illustrated by the big (Si) and small (H) spheres. The short thick bars (marked by the gate voltage V_g) indicate the position of the gates. The gate region is the supercell region between the two bars with the gate length along z. (b) The two equivalent capacitive circuits for the double gate MISFET. The surface potential V_s is the averaged potential change on the outer surfaces of the H slabs (indicated by the horizontal dashed lines in (a)) in the gate region when a gate voltage is applied. The central potential V_c is the averaged potential change on the central y-z plane in the gate region.

B. Theoretical Formalism

To analyze the electrostatic and transport properties of the atomic scale MISFET, we utilize density functional theory (DFT), [29, 30] which converts the many-body system into a single-particle system, and the two-terminal nonequilibrium Green's function (NEGF) technique [25, 31], which takes care of the coherent transport through the system between the source and the drain electrodes in Landauer picture [25, 32, 33, 34, 35]. With standard norm-conserving pseudopotentials [36] to describe the effective interaction of the valence and core electrons, we construct a localized SIESTA linear combination of atomic orbitals (LCAO) basis set $\{\psi_i\}$ [37] as the representation for expanding the electronic wavefunctions. According to the Hohenberg-Kohn theorem, [29] in the Born-Oppenheimer approximation, the fully interacting electron problem for the ground state can be mapped into a variational problem in terms of a single-particle

density $\rho(\boldsymbol{r})$. The Kohn-Sham (KS) equation [30] is then established for the atomic system in the representation $\{\psi_i\}$ with the corresponding KS Hamiltonian operator expressed in matrix form as $H[\rho(\boldsymbol{r})]$. In extending systems, we use the supercell technique with the periodic boundary condition to define and solve the KS equation in the whole real space. The dimension of the supercell is chosen larger than the screening length of the KS potential in any direction so the real system is well mimicked by that inside the supercell. In open systems, the wavefunction differs from that in closed system and this is taken care of by using the Green's function of a semi-infinite lead [38] as the boundary condition for the Green's function inside the supercell. With the KS Hamiltonian H we calculate the retarded (advanced) Green's function (GF) $G^{R(A)}(\varepsilon)$, Keldysh GF $G^{<}(\varepsilon)$ and retarded (advanced) self-energy $\Sigma^{R(A)}(\varepsilon)$. The density matrix $\rho(\boldsymbol{r})$ then reads [25, 31, 39]

$$\rho = -\frac{i}{2\pi} \int d\varepsilon G^{<}(\varepsilon). \tag{1}$$

The final density matrix is self-consistently reached from an initial guess, for which we use the neutral atom density matrix obtained by assuming no interaction between atoms. In the linear response region where the bias between the electrodes is small, the Fisher-Lee relation [40] connects the Green's functions with the transmission coefficients. With the density matrix and the Green's functions known, the transmission $T(\varepsilon)$ for the quantum transport between the electrodes is then given by [25]

$$T(\varepsilon) = Tr[\Gamma_L G^R \Gamma_R G^A], \tag{2}$$

where Γ_L, Γ_R are line-width functions of left and right electrodes which indicate the corresponding coupling strength between the electrodes and central region. The linear zero-temperature conductance is determined by the transmission at Fermi energy

$$G = (2e^2/h)T(E_F). \tag{3}$$

C. Computational Method

Atomistix ToolKit (ATK) [41] for two-probe systems together with a multigrid Poisson solver [42, 43] is used to carry out the numerical calculation. We at first apply the periodic boundary condition in the x and y directions and solve the corresponding electron density $\rho_0(x, y, z)$ and electrostatic potential $V_0(x, y, z)$. $V_0(x, y, z)$ on the boundary is denoted as the boundary condition at $V_g = 0$. The boundary condition at finite V_g is obtained by shifting $V_0(x, y, z)$ with V_g on the gate but keep the same as $V_0(x, y, z)$ on the electrodes. On each boundary region between a electrode and a gate the potential shift decreases linearly from V_g to zero. The modified boundary condition is then applied to the system to solve $\rho(x, y, z)$ and $V(x, y, z)$ at arbitrary V_g. In the calculation we use

the SZP, single ζ valence s and p orbitals (s orbitals) plus single ζ-polarization d (p) orbitals for Si (H), real space SIESTA LCAO basis set [13, 37, 41] and the standard nonlocal norm-conserving pseudopotential [36] from the database in ATK. The reason why we use the SZP basis set instead of a simpler one is because the result presented in this paper converges for SZP and more complete basis sets. The local density approximation (LDA) with the Perdew-Zunger parametrization [44] of the correlation energy for a non spin-polarized homogeneous electron gas [45] is used for the exchange-correlation functional. The mesh cutoff is set to 4348.48 eV corresponding to a grid size of 0.092Å×0.092Å×0.092Å. The MonckHorst-Pack k-point grid is $(1, 1, 100)$ along (x, y, z) directions.

III.   RESULTS AND DISCUSSIONS

To express a physical property A in our microscopic model on the same footing as its counterpart in traditional macroscopic model, we measure it from its value at $V_g = 0$ and use its average over the y-z range inside the central unit cell (8.15 Å $< z <$ 13.58 Å), $\langle A \rangle_{y,z}$, in the following analysis. The total net charge Q is the total charge transferred into the supercell when V_g is applied. Note that there may be a shift between V_g in our model and the observed in experiments because i) the real boundary condition at $V_g = 0$ may differ from the periodic (bulk) boundary condition used in the calculation, ii) the boundary potential shift when a finite V_g being applied is determined selfconsistently and can vary in different environments, and iii) no workfunction is specified for the gate metal.

Equivalent capacitive circuits are widely used in qualitative analysis of electrostatic properties of MISFETs in the literature. Our system is macroscopically symmetric about the y-z (top-down) and x-y (left-right) planes and three capacitors, C_i, C_{sz} and C_{sx} may be used for this purpose. As shown in Fig. 1(b), left circuit, C_i accounts qualitatively for the average voltage drop across the insulator slab while C_{sx} for the one across the Si slab in x direction and C_{sz} in z direction. For long channel as usually exists in traditional DG MISFETs, one-dimensional approximation is valid and only C_{sx} is important for the electrostatic analysis. For short devices, however, the boundary at the ends of the channel also plays an important role in determining the potential profile in the center of the channel and the effect of C_{sz} should be taken into account. Because only the linear region is concerned in this paper, we can also use a single capacitor C_s to describe the electrostatic properties of the Si slab with $C_s = C_{sx}C_{sz}/(C_{sx} + C_{sz}) \sim C_{sx}$, as illustrated in the right circuit of Fig. 1(b). The total net charge in the Si slab reads

$$ Q = V_g C = (V_g - V_s)C_i = (V_s - V_c)C_{sx} = V_c C_{sz}, \quad (4) $$

with the total capacitance $C = [1/C_i + 1/C_{sx} + 1/C_{sz}]^{-1}$.
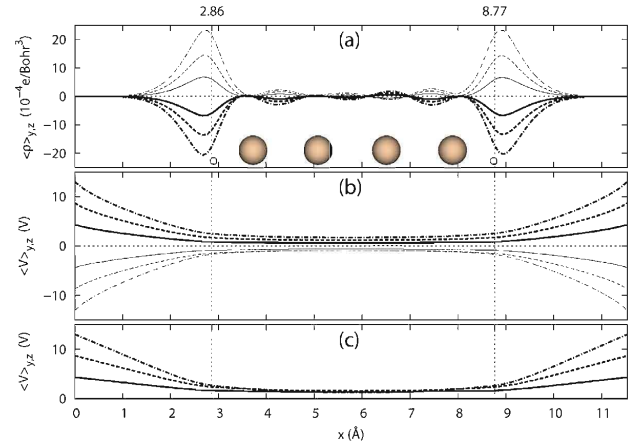

FIG. 2: (a) The charge density $\langle \rho \rangle_{y,z}$ versus the x coordinate for model S_{12}. (b) The electrostatic potential $\langle V \rangle_{y,z}$ versus the x coordinate for model S_{12}. (c) The same as (b) for model L_{12}. Curves at positive (thick) and negative (thin) gate voltages V_g of values 0.0, 4.35, 8.70, and 13.05 V are plotted as the dotted, solid, dashed, and dash-dotted respectively. The vertical dashed lines at $x = 2.86$ and 8.77 Å indicate the positions of the two surfaces between the device channel and the insulator slabs. The positions of atomic monolayers are denoted by the big (Si) and small (H) spheres. The average $\langle \ldots \rangle_{y,z}$ is done over y and z in the region $0 < y < 5.43$ Å and $8.15 < z < 13.58$Å.

Here V_s is the surface potential and V_c the central potential of the channel as further specified in Sec.III.B.

A.   Charge and Potential Distributions in Real Space

The charge density $\langle \rho \rangle_{y,z}$ distribution along the gate (x) direction is shown in Fig. 2(a) for model S_{12}. Similar distribution is observed for other models and is not plotted here. Attracted by the charge in the metal gates, most of the net charges appear near the surface of the Si slab. As a result, as illustrated in Figs. 2(b) and (c), the electric field concentrates mainly in the vacuum slab where $\langle V \rangle_{y,z}$ varies rapidly and is weak inside the Si slab where $\langle V \rangle_{y,z}$ becomes flat. The FET is in its off region at small V_g and $\langle V \rangle_{y,z}$ shifts with V_g until V_g reaches the threshold voltage where $\langle V \rangle_{y,z}$ saturates in the center of the Si slab.

An interesting short gate effect is observed when comparing the potential distribution for the short gate model S_{12} and that for the long gate model L_{12}. For the short gate model S_{12}, as shown in Fig. 2(b), $\langle V \rangle_{y,z}$ versus x in the vacuum regions ($0 < x < 2.86$Å or 8.77Å $< x < 11.63$Å) is nonlinear. This is a result of the fact that the length of the gate in model S_{12} is comparable to the thickness of the vacuum slabs in model S_{12}. The electric field in the vacuum slabs deviates greatly from along the x direction and the parallel-plate capacitor model

proportional to the inverse of it. In the on region, when a large amount of free charges are created on the surface, V_c is almost pinned due to the screening effect of these free charges.

The total net charge Q versus the gate voltage V_g for model S_{12} is shown by the dashed curve in Fig. 3(a). At $V_g = 0$, the Fermi energy E_F is located in the energy gap of the Si slab. As V_g varies, the relative position of the Fermi level in the energy band shifts accordingly. C_s remains almost constant when the Fermi level is in the energy gap but increases quickly as the Fermi level enters the conduction or the valence band. This sudden increase of C_s happens at the positive and negative threshold points, i.e., near $V_g = 13$ V and -7 V, respectively. Near these two points, due to the shift of the C_s/C_i ratio, the V_s versus V_g curve also changes its slope as shown by the dashed curve in Fig. 3(b).

To show the effect of the vacuum-slab thickness on the electrostatic characteristics, we use model S_{11} with a thinner vacuum slab and redo the calculation. $\langle\rho\rangle_{y,z}$ and $\langle V\rangle_{y,z}$ have similar profiles between the gates as that for model S_{12} but with a larger amplitude at the same gate voltage. In the equivalent capacitive circuit, C_i increases with the shrinking of the vacuum slab, which results in the shift of Q and V_s as shown by the solid curve in Fig. 3(a) and (b). The Q versus V_g curve of thicker insulator slab model S_{12} has a wider subthreshold region in the V_g axis. One interesting observation is that the threshold surface potentials, the surface potentials at the threshold points, for model S_{11} and S_{12} are very close as indicated by the short bars beside the curves in Fig. 3(b). This is because the surface potential reflects directly the Fermi level in the energy band of the Si slab. For a system of thicker insulator or smaller C_i it takes a bigger gate voltage difference to shift the Fermi energy from the valence band to the conduction band.

In Fig. 2 we have shown that the electric field in the insulator slab can deviate from normal to the slab due to the fringe effect in short gate cases. This short gate effect in nano FET reduces the per area capacitance of the insulator slab and results in a larger threshold gate voltage than estimated from parallel capacitance approximation. In Fig. 3(c) and (d) we plot the Q versus V_g curves and the V_s versus V_g curves respectively for model S_{12} (dashed) and longer gate model L_{12} (dash-dotted). The smaller total capacitance C in model S_{12}, due to its half gate length plus the short gate effect in it, results in a less than half net charge Q in the system at any V_g and a much gentler slope of its Q versus V_g curve in Fig. 3(c). In Fig. 3(d), we also observe a gentler slope of the V_s versus V_g curve for model S_{12} in the subthreshold region. Combining the relation $V_s/V_g = C_i/(C_i + C_s)$ as expressed in Eq. (4), this means a smaller ratio of C_i/C_s and confirms the conclusion drawn from Fig. 2 that the short gate effect mainly reduces the insulator capacitance.

Up to now, we have seen that both making the insulator slab thinner and suppressing the short gate effect can enhance the insulator capacitance and reduce the thresh-

FIG. 3: The total net charge Q in (a), (c), and (e) and the surface potential V_s in (b), (d), and (f) versus the gate voltage V_g are shown for models S_{11} (solid curve), S_{12} (dashed), S_{21} (dotted), and L_{12} (dash-dotted). Results for models of different insulator thickness are compared in (a) and (b), of different gate length in (c) and (d), and of different Si slab thickness in (e) and (f). The short bars beside the curves in (b), (d), and (f) indicate the V_s values at the threshold points where the V_s versus V_g curves change their slopes.

fails. For longer gate model L_{12}, the fringe effect on the channel region is reduced and the $\langle V\rangle_{y,z}$ versus x curves in the vacuum slabs become straight as shown in Fig. 2(c). The short gate effect described above is unique in nanoscale MISFET and does not appear in conventional MISFET since there the insulator slab's thickness is usually much smaller than its length. We will further discuss its effect on the FET's performance in Fig. 3(c) and (d).

B. Total Transferred Charge and Surface Potential

We use the surface just enclosing the H and Si atoms as indicated by the horizontal dashed lines in Fig. 1(a) or the vertical dashed lines at 2.86 Å and 8.77 Å for model S_{12} in Fig. 2(a) as the surfaces separating the channel and the insulator slab. The averaged value $\langle V\rangle_{y,z}$ on these surfaces is used as the surface potential V_s. The central potential V_c is approximated as the $\langle V\rangle_{y,z}$ value in the middle of the two gates, i.e. at $x = 5.82$ Å in Fig. 2(a) for model S_{12}.

With V_s and V_c known at each V_g, we can estimate the capacitance from Eq. (4). For traditional MISFETs, usually we have $C_{sx} < C_i$ in the off region and $C_{sx} > C_i$ in the on region. However, the Si slab here is extremely thin and $C_{sx} > C_i$ in both regions. In addition, the span of the device in the z direction is larger than that in the x direction. This fact leads to $C_{sx} > C_{sz}$ in the off-region and C_s may increase with the Si slab thickness because C_{sz} is proportional to the thickness while C_{sx} is

old gate voltage as illustrated in Fig. 3(b) and (d). On the other hand, a close comparison of the curves shows that the two changes to the system have opposite effects on the threshold surface potential. The threshold surface potential has a tendency to increase in the former case (the solid bar on the positive V_g side in Fig. 3(b) is slightly higher than the dashed one) while the threshold surface potential decreases in the latter case. A detailed study shows that the variation of the threshold surface potential is related to the potential distribution inside the Si slab. Given the same surface potential in the subthreshold region, the potential distribution along x changes little when varying the insulator slab thickness but a potential drop appears and broadens in the center of the $\langle V \rangle_{y,z}$ versus x curves when shortening the gate.

In Fig. 3(e) and (f), we present the dependence of electrostatic characteristics on the Si slab thickness exemplified by model S_{11} and S_{21}. Similar to the case of thicker insulator slab as shown in Fig. 3(a) and (b), the Q and V_s versus V_g curves for a system of thicker Si slab also have a wider subthreshold region in the V_g axis. However, this apparent common feature in the two cases has different origins and it is interesting to compare the details of their electrostatic characteristics.

At first, as pointed out earlier in this section, because the Si slab inside the supercell has a dimension in the z direction bigger than that in the x direction, $|C_{sx}| > |C_{sz}|$ and C_s increases with the Si slab thickness in the off-region. In this case, the Q versus V_g curve of thicker Si slab model S_{21} (dotted) in Fig. 3(e) has a sharper slope in the off-region due to an increased total capacitance C, in contrast to the gentler slope of the curve for thicker insulator slab model S_{12} (dashed) in Fig. 3(a). In addition, the bigger C_s in the thicker Si slab case, in stead of the smaller C_i as in the thicker insulator slab case, results in the gentler slope of the dashed V_s versus V_g curve in Fig. 3(f).

Secondly, it is well known [9, 46, 47] that the energy gap of semiconductor materials in nanostructures is enlarged from their bulk value as a result of the quantum confinement effect. The change of the gap depends on the confining potential profile characterized by parameters such as the confining dimension and the potential height. This effect is automatically taken into account by our NEGF-DFT model. As will be illustrated later in Sec.III.C, the thicker Si slab in model S_{21} has a narrower and shifted energy gap compared to that in model S_{11}. As a result, the subthreshold region in the V_s axis, i.e. the difference between the surface potentials at the positive and negative threshold points, of model S_{21} (3.79 V for the dotted curve in Fig. 3(f)) is narrower than that of model S_{11} (3.99 V for the solid curve). Furthermore, we also observe a shift of the subthreshold region in the V_s and V_g axes when the Si slab thickness varies.

As discussed above and illustrated in Fig. 3(e) and (f), the thicker Si slab in model S_{21}, compared to that in model S_{11}, narrows the subthreshold V_s region via the quantum confinement effect on the one hand and reduces
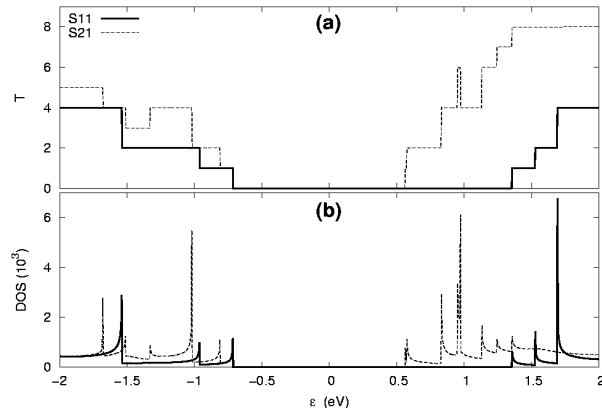

FIG. 4: (a) The transmission T and (b) the density of states (DOS) for electrons of momentum $(0,0,k_z)$ are plotted as functions of the electron energy ε in models S_{11} (solid curve) and S_{21} (dashed).

V_s/V_g ratio in the off-region due to the specific length-thickness ratio of the Si slabs in the models on the other hand. The observed wider subthreshold V_g region is a result of the competition between these two independent but opposite factors.

In this section, we analyze the electrostatic characteristics of our model nano FET in a way widely employed in the analysis of conventional MISFET. [26] Here we want to emphasize that our system (of size 2 nm) is much smaller than any of the conventional MISFETs even the smallest predicted by ITRS in its latest report. [1] As a result, our model device shows characteristics between molecular electronics and conventional electronics. For example, we observe a large slope of the Q versus V_g curve in the off region in all models which is similar to the result of the Si_4 cluster [22] but different from that in conventional MISFET where a flat Q-V_g dependence is usually found in the off region. In addition, the threshold gate voltage in our systems (> 5 V) is much higher than the value usually observed in conventional MISFET (< 2 V). This is because the Si slab in our systems is very thin and a vacuum instead of SiO_2 slab is used as the insulator slab. The C_s/C_i ratio then becomes much larger in the off region.

C. Transmission and Density of States

To explore further the origin of the electrostatic properties of nano FETs and the gate effect on transport, we calculate the transmission, which gives the conductance in the linear region via Eq. (3), and the density of states (DOS). In Fig. 4(a), the transmission of an electron propagating along the z direction is calculated at $V_g = 0$ for quantum transport between the source and
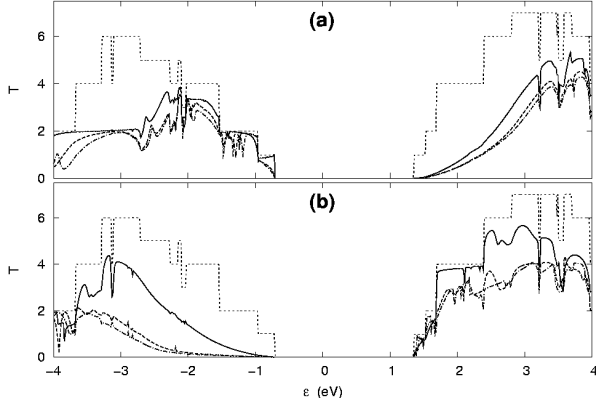
FIG. 5: The transmission T versus energy ε at $|V_g| = 0.0$ (dotted), 4.35 (solid), 8.70 (dashed), and 13.05 V (dot-dashed) is illustrated for negative V_g (a) and positive V_g (b). Model S_{11} is used in the calculation.

drain electrodes in model S_{11} (solid) and S_{21} (dashed). Because the electron sees a perfect crystal in the z direction, its transmission is 100% for each channel and the transmission versus energy curve tells the number of propagating channels for an electron of the energy. The one-dimensional DOS in k_z direction for model S_{11} (solid) and S_{21} (dashed) is plotted in Fig. 4(b). The band gap of model S_{11} is wider than that of model S_{21} due to the quantum-confinement effects in nano semiconductor structure [9]. In addition, most probably due to the change of the surface effect or the ratio between the numbers of the H and Si atoms in the system, a shift of the energy gap is observed when varying the Si slab thickness.

The transmission versus electron energy at different gate voltages is plotted in Fig. 5 for model S_{11}. When a negative gate voltage is applied, the energy band in the gate region shifts to higher energy. This shift forms an energy barrier for electrons and a well for holes. As a result, we observe a significant decrease of transmission for electrons near the bottom of the conduction band as shown in Fig. 5(a). On the contrary, if a positive gate voltage is applied, an energy barrier is formed for the holes in the middle of the device and the propagation of holes near the top of the valence band becomes unfavored. The transmission profile changes quickly with the gate voltage in the subthreshold region and then becomes less sensitive when V_c and V_s saturate at V_g higher than the threshold gate voltage.

IV.   SUMMARY

In summary, we have proposed an atomistic multi-terminal model for electrostatic simulation of nano MIS-

FETs in the framework of the NEGF-DFT approach and studied the behaviour of devices with Si slabs of one and two unit cells in thickness, with variable insulator (vacuum in this model) thickness, and with different gate length. The subthreshold region in terms of the surface potential reflects the band gap of the Si slabs and the surface potential at the threshold points remains little changed in devices of different insulator thickness. For a device with thicker Si slab, the subthreshold region in surface potential becomes narrower due to the quantum confinement effect while the subthreshold region in gate voltage becomes wider as a result of the competition between the confinement effect and the geometry effect on capacitance. In nano FETs where the gate length is comparable to the insulator thickness, the short gate effect results in a much wider subthreshold region than that observed in conventional MISFETs. This short gate effect can be suppressed by using longer gates to reduce the fringe effect on the electric field in the insulator slab.

In addition, we have calculated the band structure of Si slabs with different thickness. The density of states and the transmission probability of electrons in our nano FET system are then estimated to demonstrate the quantum confinement effect and the gating effect on transport in the linear region. The energy gap widens and shifts to higher energy when the Si slab varies from one to two unit-cells in thickness. The application of a gate voltage introduces energy barriers or wells to the carriers in the transport channel and modifies the performance the nano FETs. A negative gate voltage favors the hole transport between the electrodes while a positive one favors the electron transport.

Limited to the computation capability, our model system is still not fully realistic and is smaller than even the latest feasible MISFETs [1]. Nevertheless, our model may provide qualitative information about realistic MISFETs and serve as a prototype framework for nano MISFET simulations.

[1] See, for example, the ITRS website: http://www.itrs.net/.

[2] J. Crofton and P. A. Barnes, J. Appl. Phys. **69**, 7660

(1991).

[3] H. Wu, Y. Zhao, and M. H. White, Solid-State Electron. **50**, 1164 (2006).

[4] A. Rahman and M. S. Lundstrom, IEEE Trans. Electron Devices **49**, 481 (2002).

[5] E. Fuchs, P. Dollfus, G. Le Carval, S. Barraud, D. Villanueva, F. Salvetti, H. Jaouen, and T. Skotnicki, IEEE Trans. Electron Devices **52**, 2280 (2005).

[6] S. Ahmed, C. Ringhofer, and D. Vasileska, J. Computational Electron. **2**, 113 (2003).

[7] L. F. Register and K. Hess, Appl. Phys. Lett. **71** 1222 (1997).

[8] E. Polizzi and S. Datta,Third IEEE Conference on Nanotechnology, **1**, 40 (2003).

[9] S. Datta, *Quantum Transport* (Cambridge University Press, 2005).

[10] A. Pecchia, L. Salamandra, L. Latessa, B. Aradi, T. Frauenheim, and A. Di Carlo, IEEE Trans. Electron Devices **54**, 3159 (2007).

[11] Y. Cui and C. M. Lieber, Science **291**, 851 (2001).

[12] A. Pecchia and A. Di Carlo, Rep. Prog. Phys. **67**, 1497 (2004).

[13] José M. Soler, E. Artacho, J. D. Gale, A. García, J. Junquera, P. Ordejón and D. Sánchez-Portal, J. Phys.: CM **14**, 2745 (2002).

[14] M. H. Evans, X.-G. Zhang, J. D. Joannopoulos, and S. T. Pantelides, Phys. Rev. Lett. **95**, 106802 (2005).

[15] G. Hadjisavvas, L. Tsetseris, and S. T. Pantelides, IEEE Electron Device Lett. **28**, 1018 (2007).

[16] L. R. C. Fonseca, A. A. Demkov, and A. Knizhnik, Phys. Stat. Sol. (b) **239**, 48 (2003).

[17] L. Liu, D. Waldron, V. Timochevski, and H. Guo, Proceedings of 8th Intl. Conf. on Solid-State and IC technology, 1415 (2006).

[18] U. Landman, R. N. Barnett, A. G. Scherbakoy, and P. Avouris, Phys. Rev. Lett. **85**, 1958 (2000).

[19] M-F. Ng, L. Zhou, S-W. Yang, L. Y. Sim, V. B. C. Tan, and P. Wu, Phys. Rev. B **76**, 155435 (2007).

[20] M. V. Fernández-Serra, Ch. Adessi, and X. Blase, Nano Lett. **6**, 2674 (2006).

[21] T. Markussen, R. Rurali, A. P. Jauho, M. Brandbyge, Phys. Rev. Lett. **99**, 076803 (2007).

[22] Z. X. Dai, X. Q. Shi, X. H. Zheng, and Z. Zeng, Phys. Rev. B **73**, 045411 (2006).

[23] J. Taylor, H. Guo, and J. Wang, Phys. Rev. B **63**, 121104(R) (2001).

[24] S. H. Ke, H. U. Baranger, and W. Yang, Phys. Rev. B **71**, 113401 (2005).

[25] S. Datta, Electronic Transport in Mesoscopic Systems (Cambridge University Press, New York, 1995).

[26] N. Arora, MOSFET Models for VLSI Circuit Simulation (Springer-Verlag Wien, New York, 1993)

[27] F. G. Pikus and K. K. Likharev, Appl. Phys. Lett. **71**, 3661 (1997).

[28] G. Baccarani and S. Reggiani, IEEE Trans. Electron Devices **46** 1656 (1999).

[29] P. Hohenberg and W. Kohn, Phys. Rev. **136**, B864 (1964).

[30] W. Kohn and L. J. Sham, Phys. Rev. **140**, A1133 (1965).

[31] A. P. Jauho, N. S. Wingreen and Y. Meir, Phys. Rev. B **50**, 5528 (1994).

[32] M. Büttiker, Y. Imry, R. Landauer, and S. Pinhas, Phys. Rev. B **31**, 6207 (1985).

[33] J. Taylor, Ph.D. Thesis, McGill University (2000), J. Taylor, H. Guo and J. Wang, Phys. Rev. B **63**, 245407 (2001).

[34] M. Brandbyge, J.-L. Mozos, P. Ordejn, J. Taylor, and K. Stokbro, Phys. Rev. B **65**, 165401 (2002).

[35] Approaches of the DFT and NEGF combination used in the literature can be different depending on the assumptions, the approximations, and the basis set used in specific cases. In the paper, we specify the approach we used in this work and refer the readers to the related references for detailed analysis and justification of the approach since it has been systematically described elsewhere.

[36] D. R. Hamann, M. Schlüter and C. Chiang, Phys. Rev. Lett. **43**, 1494 (1979).

[37] P. Ordejón, E. Artacho and José M. Soler, Phys. Rev. B **53**, R10441 (1996).

[38] S. Sanvito, C. J. Lambert, J. H. Jefferson, and A. M. Bratkovsky, Phys. Rev. B **59**, 11936 (1999).

[39] B. G. Wang, J. Wang, and H. Guo, Phys. Rev. Lett. **82**, 398 (1999).

[40] D. S. Fisher and P. A. Lee, Phys. Rev. B **23**, 6851 (1981).

[41] Atomistix ToolKit Tutorial and Reference Guide version 2.0.4, Atomistix A/S (www.atomistix.com).

[42] W. L. Briggs, V. E. Henson, S. F. McCormick, *A Multigrid Tutorial*, 2nd Ed., SIAM, Philadelphia (1999).

[43] T. L. Beck, Rev. Mod. Phys. **72**, 1041 (2000).

[44] J. P. Perdew and A. Zunger, Phys. Rev. B **23**, 5048 (1981).

[45] D. M. Ceperley and B. J. Alder, Phys. Rev. Lett. **45**, 566 (1980).

[46] Y. Omura, S. Horiguchi, M. Tabe, and K. Kishi, IEEE Electron Device Lett. **14**, 569 (1993).

[47] P. V. Sushko and A. L. Shluger, Microelectronic Engineering **84**, 2043 (2007).